Structures 80 (2025) 109911

Contents lists available at ScienceDirect

Structures

journal homepage: www.elsevier.com/locate/structures

Development of a self-rising floodwall system using ultra high-performance fibre reinforced concrete

Benidir Rima [a], Farzad Hejazi [b,*], Raizal Saifulnaz Muhammad Rashid [a], Arash Rahmatian [c]

[a] Department of Civil Engineering, University Putra Malaysia, Malaysia
[b] Faculty of Environment and Technology, The University of West England, Bristol, United Kingdom
[c] Department of Computer Science and Engineering Technology, College of Sciences and Technology, University of Houston-Downtown, Houston, Houston, United States

ARTICLE INFO

Keywords:
Floodwall
Self-rising
Flood protection
Ultra-high-performance fibre-reinforced concrete (UHPFRC)
Hydrostatic pressure
Finite element analysis (FEA)

ABSTRACT

Flooding due to heavy rainfall events causes massive damage to public infrastructure and private properties, necessitating effective flood protection systems. This study develops a novel self-rising floodwall system (SRFS) which consisted of a hollow thin wall made using Ultra-High-Performance Fibre-Reinforced Concrete (UHPFRC) filled with expanded polystyrene (EPS) foam. The wall is designed to operate without the need for external mechanical power sources or sensors. The full-scale prototype of the SRFS was cast and tested in a large acrylic water tank specifically designed for this purpose, followed by an evaluation of its resistance to lateral quasi-static loads to investigate water hydrostatic pressure performance. Additionally, 3D nonlinear finite element analysis (FEA) model was developed to simulate the structural response of the floodwall under lateral hydrostatic pressure. The test results showed that the developed UHPFRC self-rising floodwall configuration exhibits the desired buoyancy characteristics, effectively floating under the upward pressure of rising water. Moreover, the wall showed excellent resistance to hydrostatic pressure. The FE analysis results agreed well with the experimental results, further confirming the floodwall's effectiveness. Furthermore, parametric studies using FE analysis were conducted to assess the influence of UHPFRC strength and wall thickness on performance of the SRFS and refining the structural design. Consequently, the increasing UHPFRC strength enhanced the wall's resistance to lateral loads. Additionally, increasing the wall thickness by 10 mm significantly improved its load-bearing capacity from 73 % to 143 %. Overall, this novel floodwall proposed in this study can provide a significant contribution to efficient floodwall protection systems.

1. Introduction

The increasing frequency and intensity of extreme weather events, such as floods, often result in significant human and economic losses [1]. These events often occur with little or no warning, making them challenging to manage and mitigate effectively [2,3]. Recent flood protection systems range from permanent barriers with underground cut-off walls to temporary and demountable structures offering varying levels of protection against these alarming events [4–7]. Permanent flood barriers offer excellent protection due to their underground cut-off barriers, which effectively control seepage, a feature lacking in temporary barriers [8]. While this system's independence from operational systems reduces failure risks, its high cost and obtrusive nature limit its practicality, especially in regions with low flood risk [9]. In contrast, temporary barriers are flexible enough to be quickly erected anywhere, relatively inexpensive, and easily stored. However, this system's drawback is high seepage rates. Demountable systems offer improved seepage control but come with higher costs and reduced flexibility compared to fully mobile flood barriers [6,10].

For flood mitigation strategies, sandbags are commonly used but are ineffective against high-velocity floods and require labor-intensive, time-consuming setup [7,9]. Other solutions, such as dike systems and mobile flood protection walls, can be effective in certain situations but face limitations in urban settings, where spatial constraints and the need for unobstructed access often complicate their implementation [3,11]. Recent advancements, such as self-closing flood barriers (SCFB), which use the approaching floodwater to automatically raise the barrier, and smart flood barriers (SFB), can address these limitations by incorporating automated features or pre-installed components into the system [1,12–14]. However, such systems still need infrastructure, complex

* Corresponding author.
E-mail address: farzad.hejazi@uwe.ac.uk (F. Hejazi).

https://doi.org/10.1016/j.istruc.2025.109911
Received 26 April 2025; Received in revised form 23 July 2025; Accepted 7 August 2025
Available online 23 August 2025

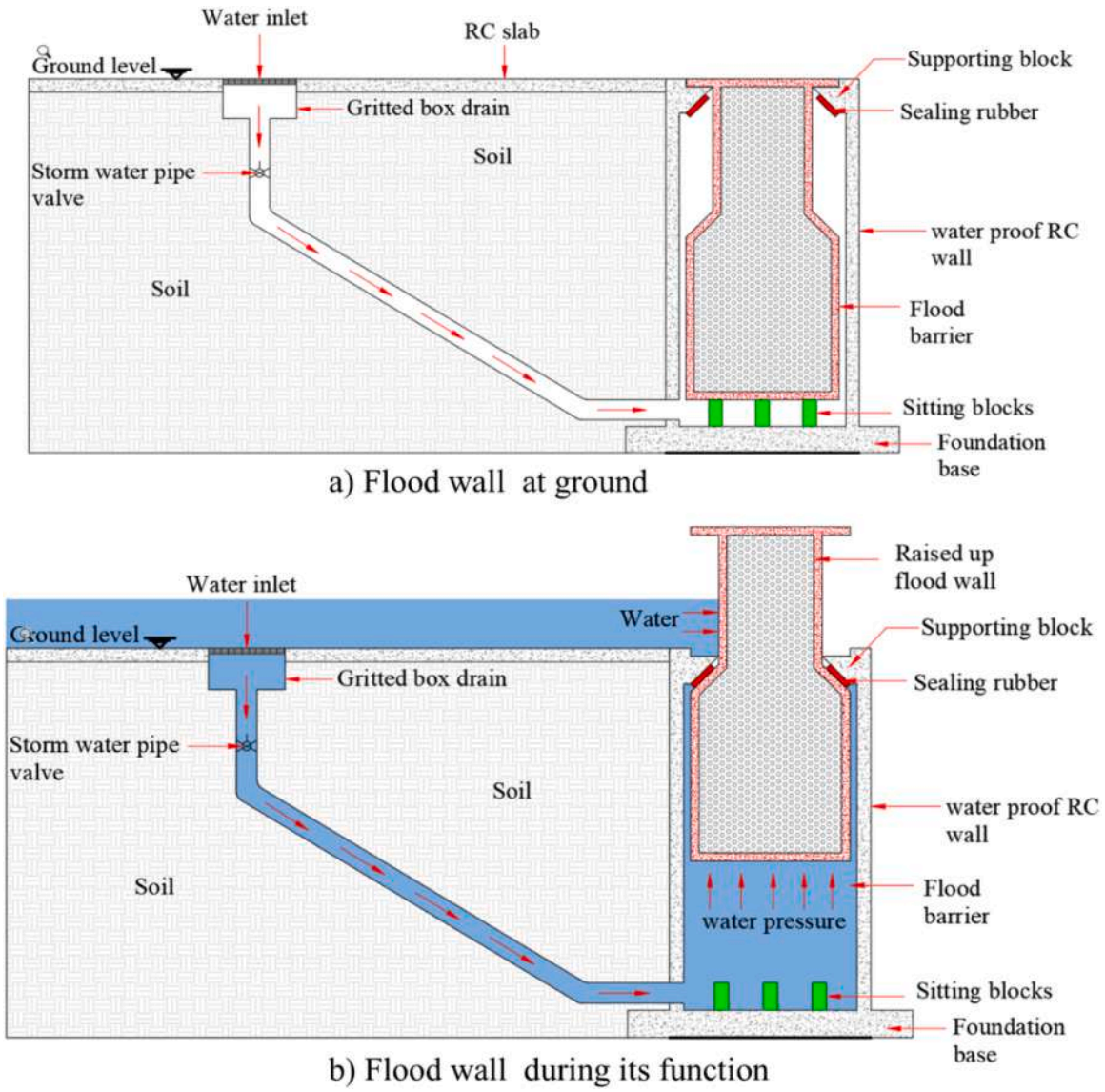

Fig. 1. Developed self-rising flood system at rest and function.

configuration and assembly, or operational power, which limits their efficiency and affordability in large-scale or diverse environmental contexts.

Several efforts have been made by many researchers to evaluate the effectiveness of barrier designs, through experimental and simulations investigations. Baiz [14] developed smart wall system using fibre reinforced concrete (FRC) uses interlocking boxes that automatically connect when extended and evaluate its performance under static and impact load. Krishnan [15] conducted a 3D finite element analysis using ANSYS to evaluate a proposed self-closing flood barrier composed of aluminum and filled with polystyrene. Rappazzo and Aronica [6] used a 2D hydrodynamic model to replicate Barcelona's 'dry proofing' flood measures, demonstrating that such barriers can significantly mitigate flood risks. Al-qaisi and Al-rammahi [16] employed parametric simulations using ANSYS to optimize floodwall barrier cross-sections, balancing resistance to hydrodynamic forces with economic efficiency, identifying best profile section for stability and cost. Similarly, Petrů et al. [17] experimentally and numerically evaluated proposed mobile flood barrier performance under real flood condition. Petru et al. [18] again developed light-weight, cost-effective, easy install anti-flood barrier and evaluated experimentally and numerically. Srb et al. [19] employed the Coupled Eulerian-Lagrangian (CEL) approach in Abaqus to simulate barrier deformation under dynamic hydrodynamic impacts. Gupta et al. [4] tested various barrier configurations in a flume, concluding that a low-height steel frame with high-quality fibre reduced risks of overturning and leakage.

Considering the above, despite the widespread implementation of various flood barriers, efficiency and effectiveness in mitigating flood risks remain challenges. This study introduces a novel self-rising floodwall system (SRFS) utilizing lightweight ultra-high-performance fibre-reinforced concrete (UHPFRC). The developed SRFS offers power-independent, easily installable, and fully automatic operation, suitable for various settings without lateral support. This research involved developing and optimizing the floodwall's configuration and dimensions. A non-linear finite element analysis (FEA) was conducted. Subsequently, The SRFS's rising mechanism was tested under upward pressure from rising water, followed by experimental testing to evaluate its resistance to lateral quasi-static loads to validate the FE model. Finally, a parametric study using FE examined the influence of UHPFRC strength and wall thickness.

2. Self-rising UHPFRC flood barrier development

The self-rising flood barrier is designed using ultra-high-Performance

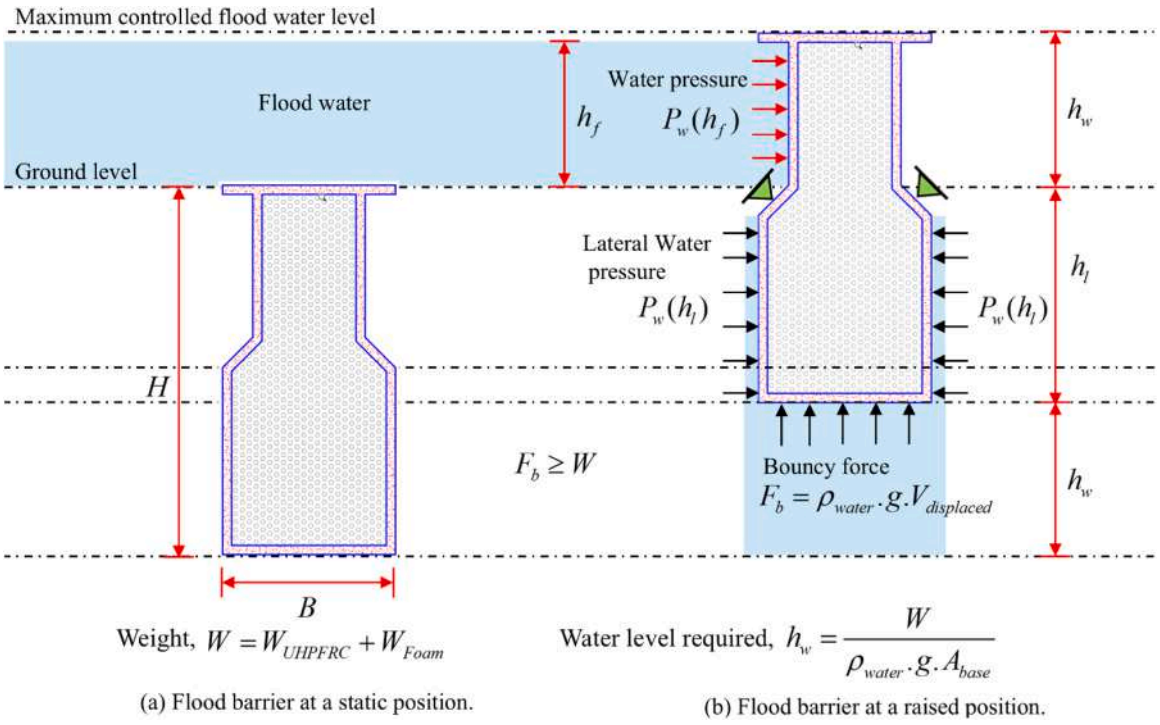

Fig. 2. Mathematical model of self-rising flood system function mechanism.

fibre reinforced concrete (UHPFRC) to ensure excellent durability and performance while maintaining a lightweight structure. The high strength and durability of UHPFRC have also led to its consideration for other demanding applications, such as floating structures for offshore wind turbines [20]. As shown in Fig. 1(a), the system comprises a self-rising floodwall made of UHPFRC, with the hollow section filled with expanded polystyrene foam. This wall barrier is placed within a sealed chamber constructed from impermeable normal-strength reinforced concrete. The chamber is provided by sitting blocks below the floodwall and is sealed with rubbers at the top of the chamber, which minimize friction damage, prevent leakage, and enhance stability. The inlet water is connected to the chamber through the designed pipe for this purpose. This pipe incorporates a gritted box drain and a stormwater pipe valve strategically placed below the water inlet. This configuration prevents water pressure backflow and protects the surrounding soil supporting the wall from erosion. Additionally, the drainage system is positioned at a safe distance from the wall to mitigate any potential damage caused to the soil foundation during operation.

The proposed protective flooding wall system remains in its static position under normal conditions, with the wall resting beneath the ground on sitting blocks, as shown in Fig. 1(a). During a flood event, water begins to accumulate and is directed through a drainage system, where a portion flows into pipes connected to the chamber cell. As water enters the chamber, its rising level and the engineered gradient create pressure that lifts the wall to its designated position. At this stage, the wall effectively blocks lateral floodwaters and provides sufficient resistance to the hydrostatic pressure. Fig. 1(b) illustrates the functional concept of the floodwall during a flood event, demonstrating its capability to control flooding effectively.

The operation of the system is fully automated, and activated as water flows into the chamber, leveraging the novel lightweight design achieved through UHPFRC and polystyrene foam filling the hollow space within the floodwall barrier. The mechanism of the proposed self-rising flood barrier, as well as the equations governing its buoyant behaviour, are rooted in the principle of buoyancy. This principle enables the flood barrier to rise naturally in response to increasing water levels.

The weight of the wall and the polystyrene foam must be in equilibrium with or less than the buoyant force exerted by the water to sufficiently lift the barrier and maintain its firm position while blocking the floodwater. As shown in Fig. 2, this buoyant force, acting primarily at the bottom surface of the wall, is determined based on Archimedes' Principle, as given in Eq.1.

$$F_b = \rho_{water} .g. V_{diplaced} \tag{1}$$

Where ρ_{water} is the water density is typically taken as 1000kg/m^3; $g$is the gravity acceleration which approximately taken as 9.81m/s^2;$V_{diplaced}$ is volume of water displaced by the submerged portion of the barrier.

The volume of water displaced is determined according to the expression given in Eq. 2.

$$V_{diplaced} = A_{base}.\mathrm{h_w} \tag{2}$$

Where A_{base} is the area of the bottom based on the floodwall; $\mathrm{h_w}$ is the water level required to lift the barrier at the firmed position.

The barrier rises as long as buoyant force F_b, equals or exceeds the gravitational force acting on it from the barrier. This gravitational force which is the weight $W$of the barrier, which resists upward movement, is determined by the total mass and gravity according to Eq. 3.

$$W = \rho_{UHPFRC}.\mathrm{g}.V_{UHPFRC} + \rho_{EPS}.\mathrm{g}.V_{EPS} \tag{3}$$

Where ρ_{UHPFRC} is the density of the UHPFRC that is typically taken as 2800kg/m^3; $g$is the gravity acceleration; V_{UHPFRC} is the volume of UHPFRC floodwall; ρ_{EPS} and $V_{EPS}$are the density and volume of the expanded polystyrene foam, respectively.

According to Eq.1 and Eq. 3, for the barrier to start rising, the net force on the barrier F_{net}must be positive (upward) which can be determined based on Eq. 4.

$$F_{net} = F_b - W \tag{4}$$

When $F_{net} > 0$, the barrier wall begins to move up. The barrier stabilizes at an equilibrium point where the buoyant force equals the gravitational force ($F_b - W = 0$), showing that the floodwall has risen to a level where

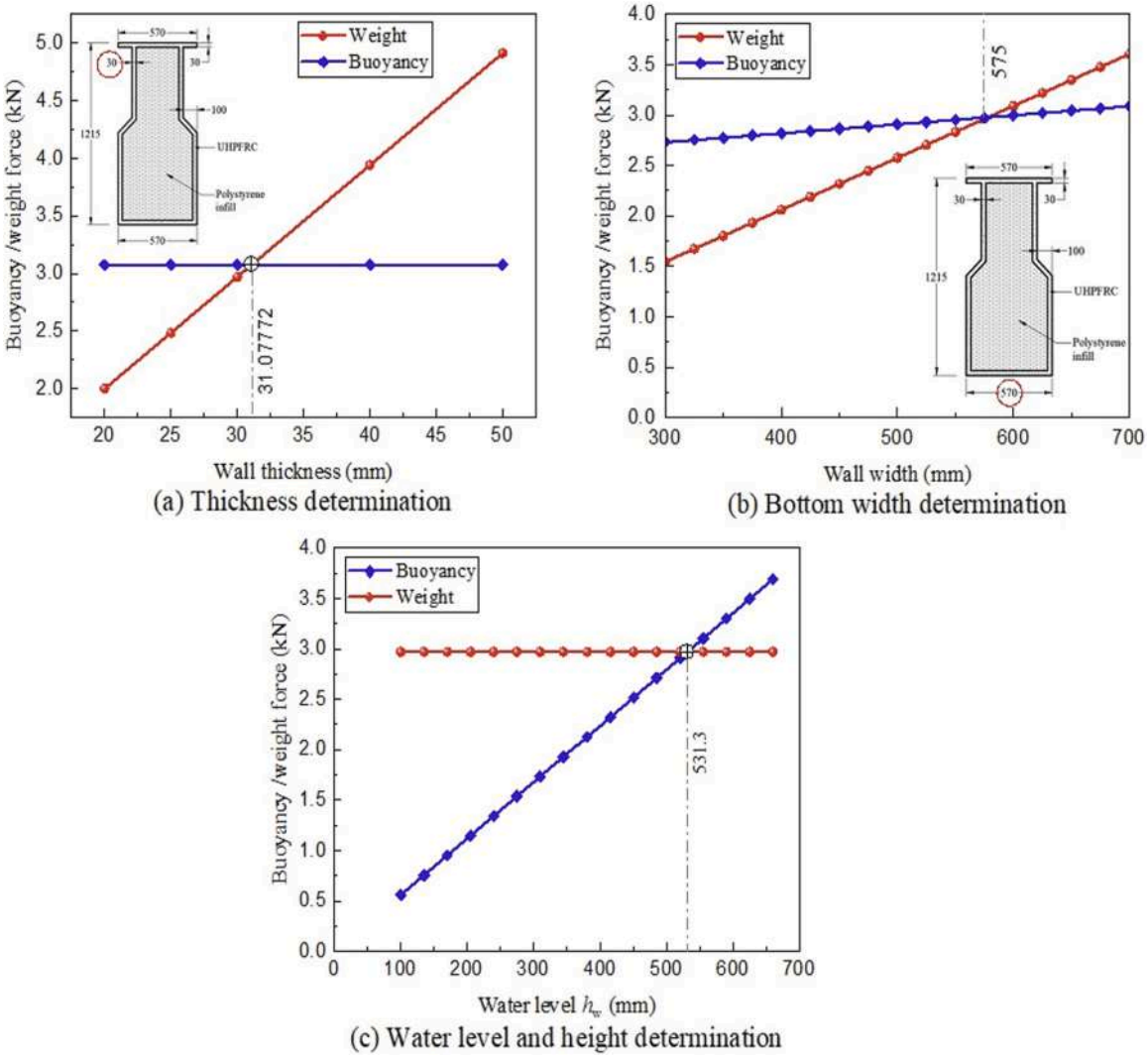

Fig. 3. Floodwall dimension determination and optimization.

the volume of displaced water provides just sufficient buoyant force to resist the weight.

To determine the required water level to sufficiently raise the barrier wall and provide the necessary displaced volume$V_{diplaced}$ (Eq.2), the water level$h_w$is defined based on the equilibrium condition, where the buoyant force equals the gravitational force, as expressed in Eq. 5.

$$h_w = \frac{W}{\rho_{water} \cdot g \cdot A_{base}} \tag{5}$$

Once, the buoyant force has raised the barrier wall to the required position and kept it firm, the flood barrier wall will act as a lateral flood block and control the flood water. The hydrostatic pressure acting laterally on the barrier wall is given by Eq. 6.

$$P_{water} = \rho_{water}.g.h_f \tag{6}$$

Where P_{water} is the flood water hydrostatic pressure; h_f is the height of the floodwall.

The total lateral force acting on the wall can be defined as the integral of this pressure over the lateral area of the wall in contact with the water, as given in Eq.7.

$$F = \int_0^{h_f} P_{water}(h_f)\,dA = \int_0^{h_f} (\rho_{water}.g.h_f)\,dA \tag{7}$$

Where dA is the differentiation contact area of the barrier with flood water.

By balancing these forces and ensuring the barrier's weight aligns with the buoyancy design, the self-rising mechanism effectively provides lateral, reliable flood protection. Fig. 3(a-c) illustrates the dimensions' optimization of the floodwall based on the intersection of the wall weight and buoyancy forces for wall thickness, wall width, and water level. As shown in Fig. 3(a), as the wall thickness increases, the weight of the wall increases linearly, while the buoyancy force remains constant. The intersection point (31.07 mm) represents the optimal wall thickness, where the buoyancy force equals the wall weight. Beyond this point, the weight of the wall becomes higher than the buoyant force, which prevents the buoyancy force from lifting the wall. Therefore, while a thickness below 31.07 mm is feasible for this configuration, a thickness of 30 mm is adopted in this study to ensure both durability and strength.

On the other hand, as shown in Fig. 3(b), increasing the wall width leads to a linear increase in both the weight and buoyancy force. The optimal width occurs at 575 mm, where the wall weight intersects the buoyancy force. Based on this, the bottom width was taken as 570 mm in this study to ensure enough contact area for the buoyancy force.

Referring to Fig. 3(c), maintaining a constant wall weight while varying the displaced water level demonstrates that the required water level is 531.3 mm, where the buoyancy force equals the weight of the

Table 1
Mixture proportions of DURA® – UHPFRC.

Component	Cement (kg/m^3)	Silica fume (kg/m^3)	Sand (kg/m^3)	Water (kg/m^3)	Superplasticizer (kg/m^3)	Steel fibre (kg/m^3)
Proportion	850	200	1030	170.9	28	118

Table 2
Mechanical properties of steel fibres.

Density (kg/m^3)	Fiber type	Diameter (mm)	Length (mm)	Aspect ratio	Tensile strength (MPa)
7867	Straight	0.2	20	100	2500

Table 3
Ultimate concrete compressive strength of UHPFRC.

Cube specimens	Days	Ultimate compressive strength (MPa)	Average Ultimate compressive strength (MPa)
1	7	66	68.33
2		67	
3		72	
4	14	80	82.567
5		82	
6		85.7	
7	28	90	91.07
8		90.5	
9		92.7	

wall. Therefore, based on Fig. 2 and Fig. 3(c), the wall height was designed to be 1210 mm to obtain optimal performance, ensuring sufficient buoyancy to lift the wall and resistance against flooding during the second stage. To minimize the weight of the wall while maintaining durability, and strength, and achieving sufficient buoyancy to lift the wall, the wall was narrowed by 100 mm on both sides above a height of 615 mm to provide an optimized configuration of the wall shown in Fig. 5.

3. Experimental program

3.1. Materials preparation

This section presents the materials used in the experimental construction of the flood barrier, which was composed of ultra-high-performance fibre-reinforced concrete (UHPFRC) and crushable expanded polystyrene (EPS) foam. The UHPC premix manufactured by DURA Technology Sdn Bhd (Malaysia), consisting of ordinary Portland cement, silica fume, and silica sands, was used to cast the floodwall. The mix also incorporated 1.5 % steel fibres, along with the appropriate amounts of water and a superplasticizer. Table 1 provides the mixture proportions of UHPC with a steel fibre content of 1.5 % used in this study, while Table 2 gives the properties of the steel fibres. Preparing fresh UHPC was carried out using a 30-L capacity planetary mixer. During this process, all the constituents were precisely measured and weighed. The premix was amalgamated for two minutes, followed by the addition of 90 % water and 100 % admixture, and mixed for five minutes until the premix agglomeration became apparent. Subsequently, the remaining 10 % water was added and mixed for three minutes. Finally, 1.5 % steel fibers (by volume) were gradually added and mixed for five minutes.

Nine concrete cube samples, each measuring 150 mm × 150 mm × 150 mm, were cast and cured in a curing tank for 7, 14, and 28 days before undergoing compressive strength tests. The ultimate compressive strength of three UHPFRC cube specimens measured at 7, 14, and 28 days is presented in Table 3. The average compressive strength at 7 days was 68.33 MPa, which increased by 21 % (82.567 MPa) at 14 days, and by the 28th day, the strength increased by 10 %, reaching an average ultimate strength of 91.07 MPa. The compressive strength obtained at 28 days does fall below the commonly accepted threshold for UHPC classification (typically ≥ 150 MPa as per AFGC and FHWA guidelines [21,22]). The mix design used was based on DURA Technology's UHPC premix; however, it is acknowledged that the achieved strength reflects high performance concrete (HPC) rather than ultra high-performance concrete (UHPC). This discrepancy may be attributed to field casting conditions, mixing limitations, or curing inconsistencies.

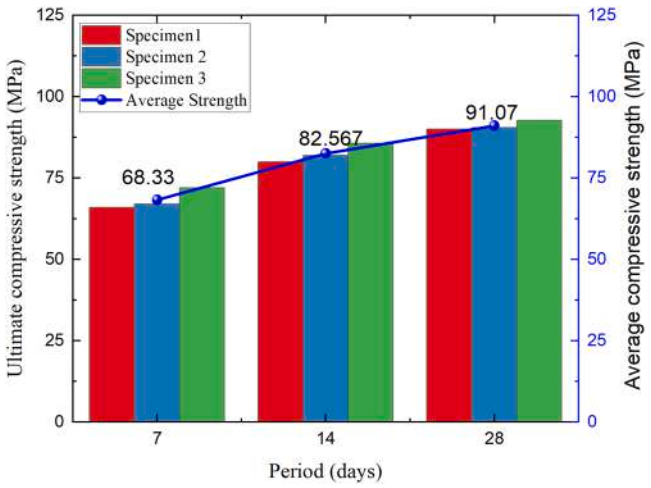

Fig. 4. Compressive strength development of UHPFRC.

Fig. 4 graphically demonstrates the ultimate compressive strength of UHPFRC, along with the average ultimate compressive strength developed over the curing period.

On the other hand, expanded polystyrene (EPS) foam was selected for its lightweight and energy-absorbing properties during wall function. The foam used in this study had a density of 12.7 kg/m^3 and a Young's modulus of approximately 2.2 MPa, as reported by [23] making it suitable for filling the hollow spaces within the flood barrier. It was prepared by cutting the foam into precise dimensions to ensure a precise fit within the wall cavity.

3.2. Specimen preparation

The flood barrier was pre-dimensioned based on Archimedes' principle of buoyancy. The resulting dimensions were a total height of 1215 mm, a width of 570 mm, and a length of 1000 mm. The specimen consisted of a hollow section with a 30 mm-thick UHPFRC layer, filled with EPS. The general details of the specimen prepared in this study are shown in Fig. 5.

The external framework of the specimen was constructed using plywood, as shown in Fig. 6(a). The EPS panels were cut to the specified dimensions and glued and secured into the formwork (Fig. 6(b)). Moreover, to ensure the EPS remained level during the casting process, boards were attached over the core to prevent slipping or floating due to fresh concrete being poured on top (Fig. 6(c-d)). The concrete was carefully poured into the formwork, filling the voids between the external wood framework and the EPS foam, as shown in Fig. 6(e). During this process, the concrete was directed into all corners and gaps to ensure uniform distribution and prevent void formation. The specimen was then covered with a plastic sheet and stored at room temperature for 24 h. Subsequently, the wooden framework was removed from the mould, and the specimen was cured under standard curing conditions for 28 days, as shown in Fig. 6(f).

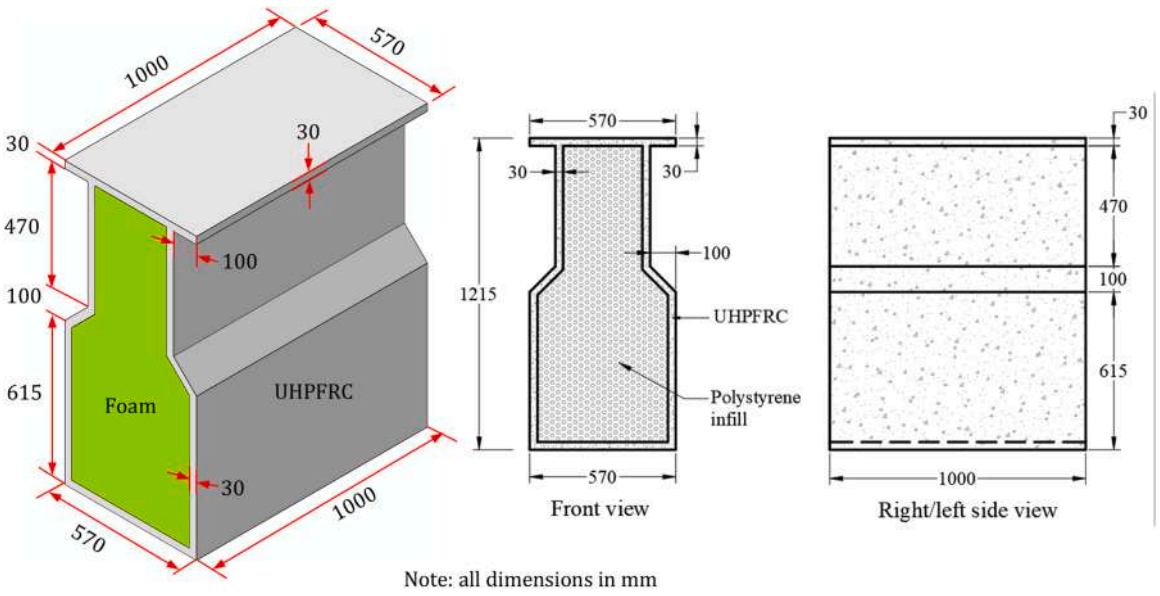

Fig. 5. Geometrical details and configuration of the UHPFRC sandwich floodwall.

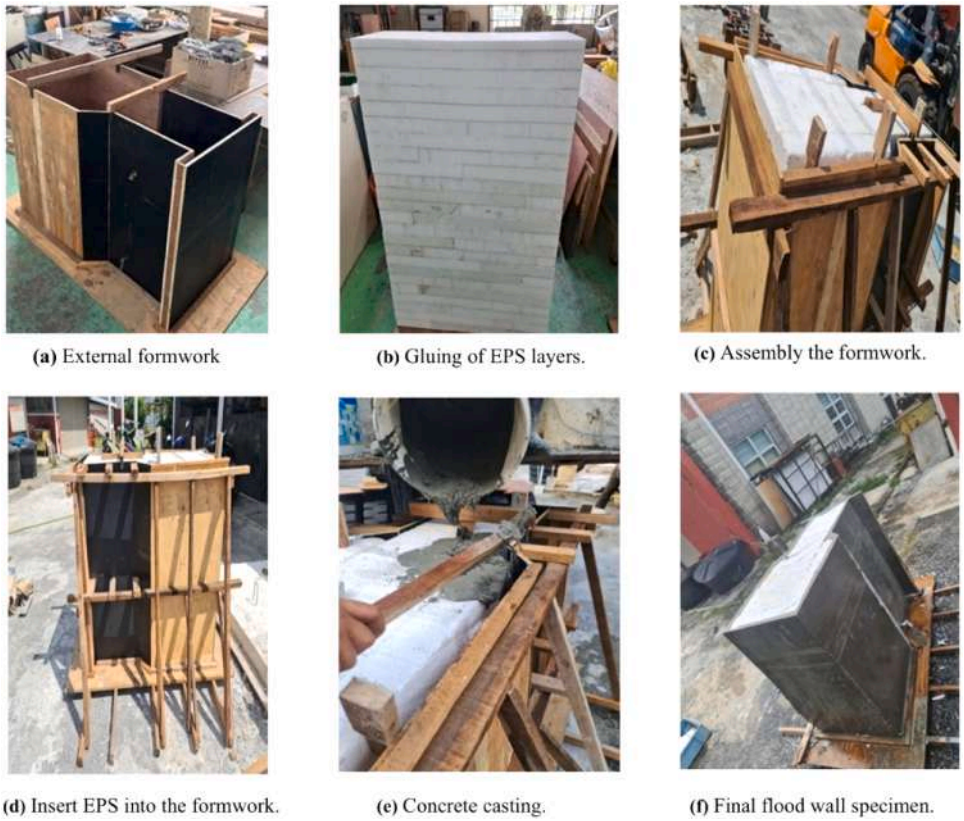

Fig. 6. Floodwall specimen preparation.

3.3. Experimental set-up

Two setups were implemented in this study: the first for the buoyancy test and the second for the lateral quasi-static test.

3.3.1. Buoyancy test-setup

To facilitate the buoyancy assessment prior to the lateral quasi-static testing of the floodwall developed in this study, a custom water chamber was constructed from 10 mm thick acrylic sheets to ensure efficient function and cost-effectiveness, with a height of 1.1 m (Fig. 7(a)). To minimize the bending deformation of the acrylic panels, a steel frame was designed on the outside (Fig. 7(b)). The edges of the box were sealed internally with silicone. Moreover, a fitting valve with a diameter of 25 mm was installed on both sides, ensuring the water to be sealed and allowing the box to empty in short time (Fig. 7(c)).

The floodwall specimen was carefully positioned within the steel-framed acrylic box using a crane to ensure precise placement. Water was introduced into the acrylic box through a fitting valve, gradually

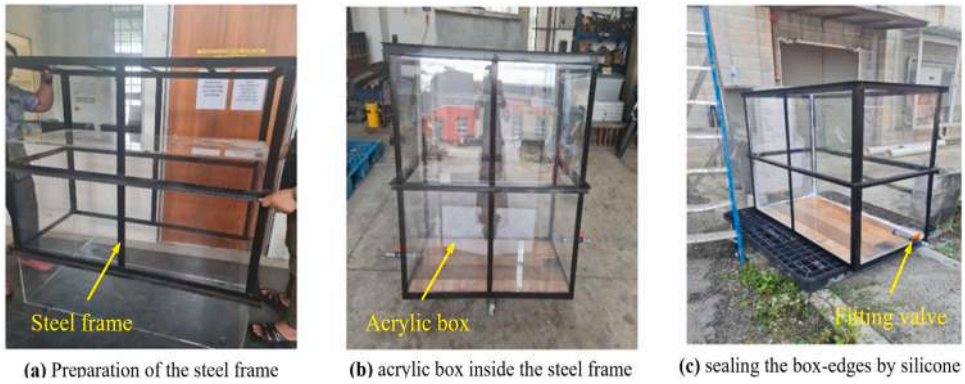

Fig. 7. Preparation of the chamber water box.

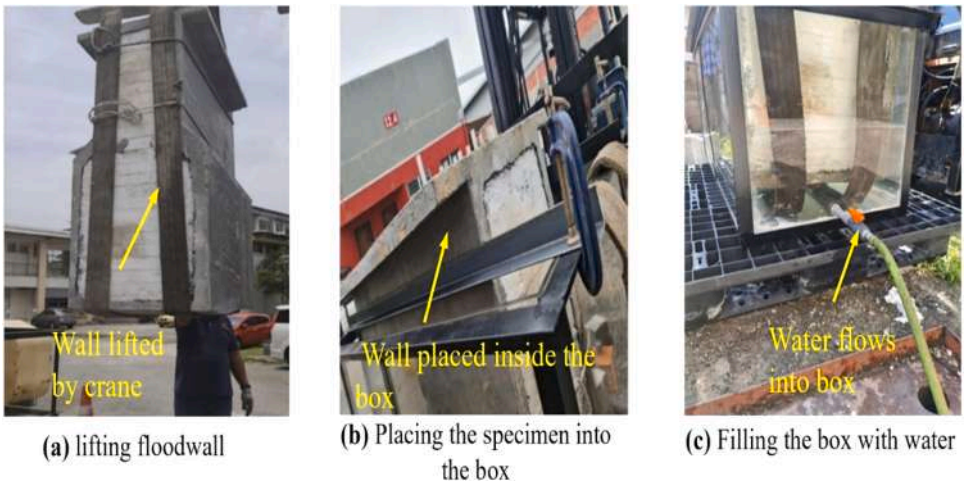

Fig. 8. Buoyancy test set-up.

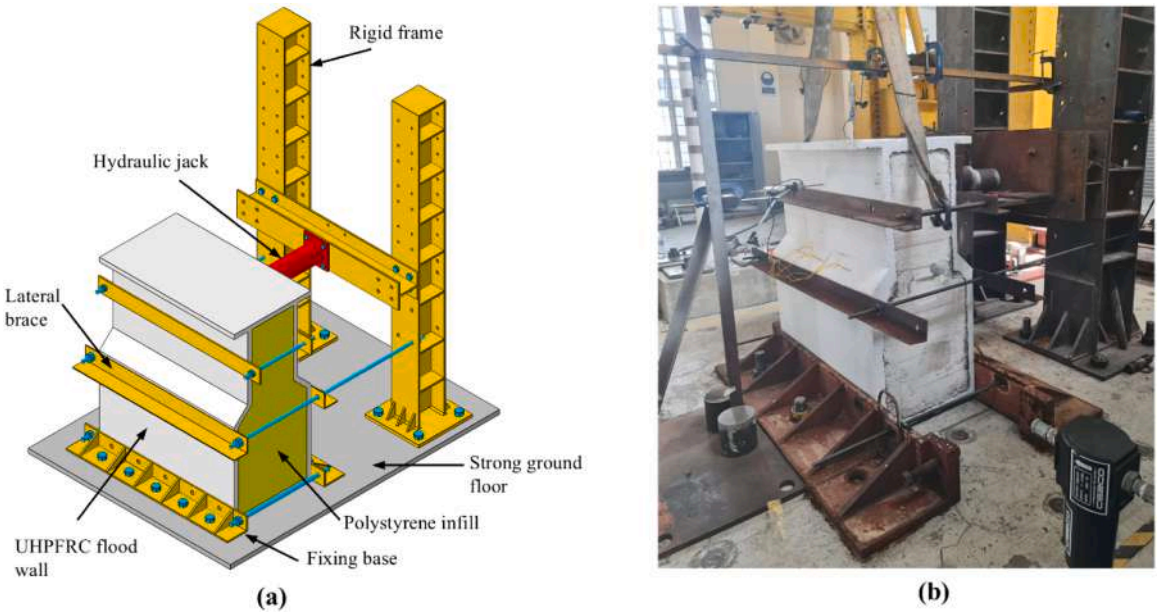

Fig. 9. (a) 3D schematic diagram of the setup; (b) Experimental setup in the laboratory.

increasing the water level to elevate the floodwall within the box. The buoyancy test setup details are illustrated in Fig. 8(a–c).

3.3.2. *Lateral quasi-static test setup*

To test the specimen under a quasi-static lateral load. The bottom of the specimen was firmly fixed to the rigid floor using two steel angles

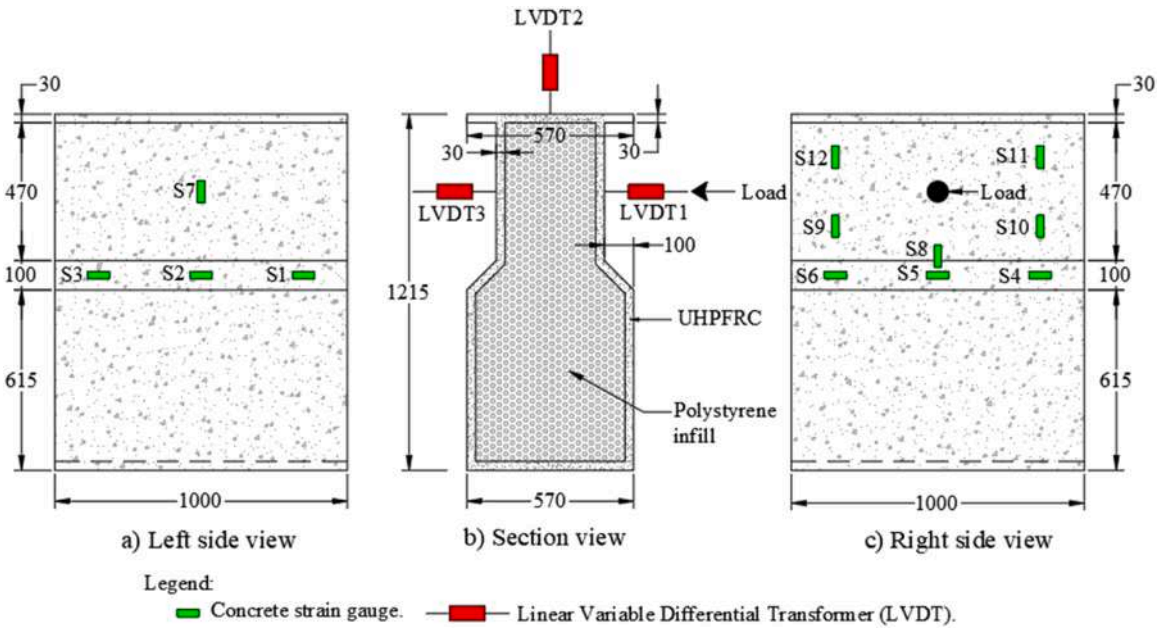

Fig. 10. Installation of LVDTs and strain sensors.

Fig. 11. Rising of the proposed floodwall under the normal water pressure.

bolted to the ground. These two steel angles were securely fastened horizontally using two bolted bars. Furthermore, two steel angles were placed 615 mm above the bottom of the wall and fastened horizontally with two long bars connected to the loading frame to simulate the role of sealing rubber in preventing horizontal movement (Fig. 9(b)). It is noted that the lateral brace in the experimental setup was positioned below the sealing rubber level shown in Fig. 1 due to laboratory constraints and to facilitate stable load application through the hydraulic jack. Although this variation may slightly influence the load distribution and deformation response, the brace effectively restrained out-of-plane displacement and simulated lateral resistance. The floodwall was subjected to lateral quasi-static loading, representing the hydrostatic pressure, using the displacement control method. The displacement was applied at a constant rate of 0.01 mm/minute and gradually increased until the failure of the floodwall. The lateral loading was applied using a hydraulically actuated jack with a 1000 KN load capacity, positioned horizontally on a steel plate located 945 mm above the base of the wall. This steel angle, connected to the opposing angle through two bolts, served to evenly distribute the load from the hydraulic jack across the top of the floodwall. Fig. 9(a) shows the 3D schematic diagram of the setup, while Fig. 9(b) illustrates the experimental setup in the laboratory.

As shown in Fig. 10, several linear variable differential transformers (LVDTs) and strain gauges were installed at specific locations on the test specimen to continuously measure deflection and strain.

3.4. Experimental results and discussion

As previously mentioned, the specimen was subjected to both buoyancy testing and lateral quasi-static loading. This section provides a detailed discussion of the results of these two tests.

3.4.1. Self-rising functionality results

Fig. 11 illustrates the results of the self-rising functionality (buoyancy test) results conducted on the proposed floodwall, where the water displaced the flood barrier nearly 200 mm in height, generating sufficient buoyant force to counteract the weight of the wall. This outcome confirms that the design effectively meets the intended performance criteria under the limited conditions of the test setup.

3.4.2. Lateral quasi-static load test results

3.4.2.1. Failure modes. The failure mode of the UHPFRC flood barrier subjected to lateral quasi-static load is shown in Fig. 12. The specimen remained uncracked until the load reached 6 kN, with a corresponding displacement of 1.7 mm, at which point the first hairline crack was observed at the top far-left corner of the loaded face, extending 50 mm in length (Fig. 12(a)).

At 12.7 kN, another hairline crack emerged 200 mm from the left side of the loaded face and propagated diagonally, reaching a length of 100 mm. As the load increased to 20 kN, a flexural crack developed at the joint transition zone and extended further, eventually reaching a length of approximately 250 mm at the failure load (Fig. 12(a)). On the other hand, a combination of diagonal and horizontal cracks developed and propagated within the weak transition zone between the widened and narrowly spaced regions on the opposite face of the wall, as shown in Fig. 12(b). Overall, the cracking pattern indicates that the failure mode of the specimen was characterized by flexural failure.

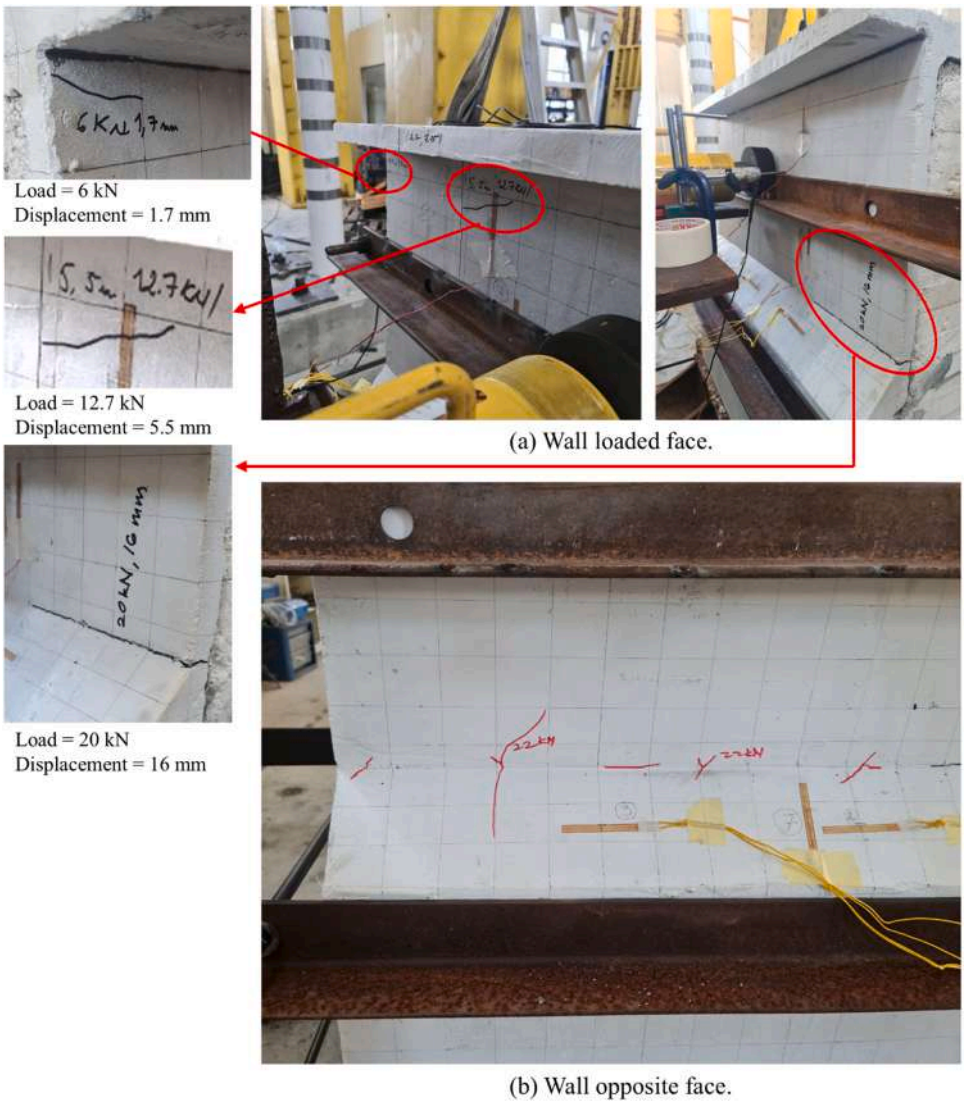

Fig. 12. Specimen failure model under lateral quasi-static load.

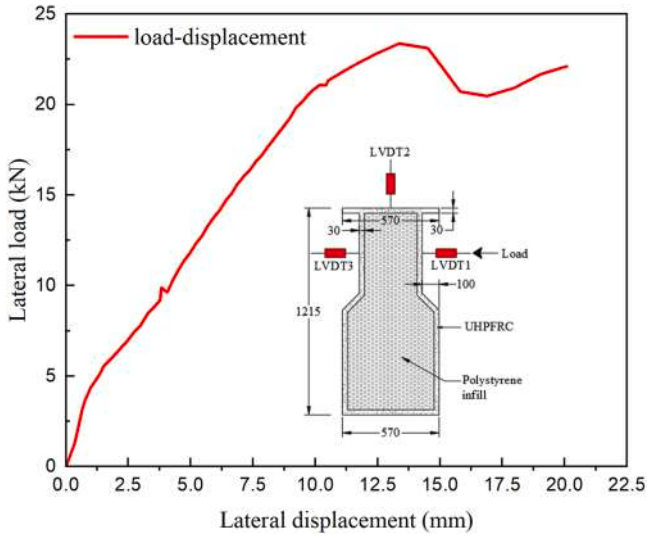

Fig. 13. Lateral load-displacement response of the specimen.

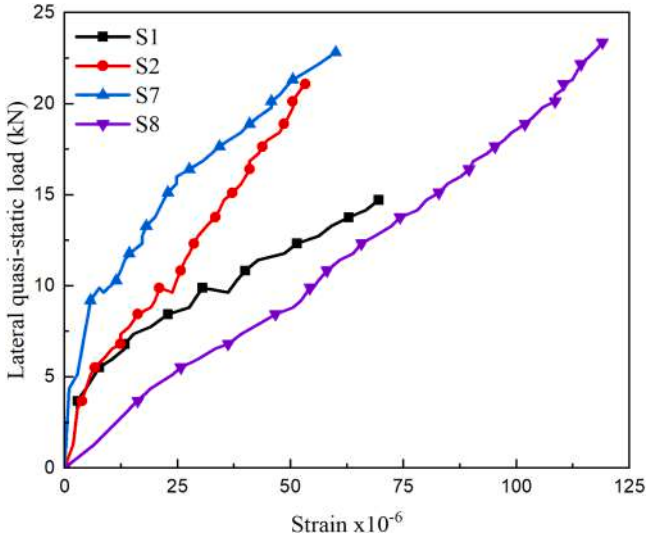

Fig. 14. Strain response of the UHPFRC floodwall subjected to lateral quasi-static load.

3.4.2.2. Load-deflection response. Fig. 13 illustrates the load-displacement response of the floodwall subjected to a quasi-static load. The specimen exhibited an almost linear behaviour up to 5 kN, approaching the cracking load of 6 kN with a corresponding displacement of 1.7 mm. Beyond this point, the specimen exhibited nonlinear behaviour, continuing until it reached the yield load P_y of 21.07 kN with a corresponding displacement of 10.16 mm. During this stage, the formation of micro-cracks was observed on the loaded face of the floodwall. After the yield load, the ultimate strength of the specimen, Pu, was attained at 23.36 kN (1.12 P_y) with a corresponding displacement of 13.36 mm. Subsequently, the strength of the specimen decreased, reaching 20.48 kN at a displacement of 16.88 mm. At this stage, the fibres within the concrete contributed to bridging and hardening, allowing the load to increase to 22.11 kN with a displacement of 20.07 mm. Additionally, the EPS is expected to have provided a minor contribution to the post-cracking load-bearing capacity by enhancing internal confinement and structural integrity. As the contributions from both the fibres and EPS diminished, a progressive reduction in strength was observed.

3.4.2.3. Strain response. Fig. 14 shows the strain of the UHPFRC floodwall subjected to quasi-static load. The strain readings were taken from S1, S2, and S7, located on the opposite face, while S8 was taken from the strain gauge located on the loaded face. The ultimate strains in the opposite face were69.5×10^{-6}, 53.3×10^{-6} and 60×10^{-6} for S1, S2, and S7, respectively. On the other hand, the floodwall on the loaded face was subjected to higher strain, as obtained in S8, where the ultimate strain 119.05×10^{-6} is almost twice that obtained on the opposite face of the floodwall. This is attributed to the location of S8 at the inflection point, where the strain concentration was highest. Overall, the strain readings were extremely small on both the loaded face and the opposite face. This can be attributed to the relatively low crack elongation capacity of the concrete. In contrast to actual UHPC which typically exhibits a crack elongation of approximately 0.2 per mille, the material analysed in this study behaved more similarly to conventional high-strength concrete, with an estimated crack elongation of around 0.1 per mille. Consequently, the wall showed limited post-cracking deformation capacity and maintained stiff under lateral loading.

4. Non-linear finite element modelling

To evaluate the performance of the floodwall barrier under lateral quasi-static loading, three-dimensional FE models were developed to simulate the floodwall's behaviour under such conditions.

4.1. Concrete damaged plasticity (CDP) model

The CDP model available in FE software Abaqus [24] is used to model the behaviour of the UHPFRC material. This model is first developed by Lubliner et al.[25] and later modified by Lee and Fenves [26] to account for the response of concrete under cyclic and dynamic loading conditions. Eq. 8 and Eq. 9 present the yielding criteria and the model parameters, respectively.

$$F = \frac{1}{1-\alpha}\left(\bar{q} - 3\alpha\bar{p} + \beta\left(\tilde{\varepsilon}^{pl}\right)\langle\hat{\sigma}_{\max}\rangle - \gamma\langle -\hat{\sigma}_{\max}\rangle\right) - \bar{\sigma}_c\left(\tilde{\varepsilon}^{pl}\right) \leq 0 \tag{8}$$

$$\beta\left(\tilde{\varepsilon}^{pl}\right) = \frac{\bar{\sigma}_c\left(\tilde{\varepsilon}^{pl}\right)}{\bar{\sigma}_t\left(\tilde{\varepsilon}^{pl}\right)}.(1-\alpha).(1+\alpha); \alpha = \frac{(\sigma_{b0}/\sigma_{c0}-1)}{2(\sigma_{b0}/\sigma_{c0}-1)}; \gamma = \frac{3(1-K_c)}{2K_c-1} \tag{9}$$

Where α and γ are dimensionless material constants controlled by the parameters σ_{b0}/σ_{c0} and K_c defined below, $\bar{p}$ is the hydrostatic pressure based on effective stresses, $\bar{q}$ is the effective von Mises equivalent stress, $\hat{\sigma}_{\max}$ is the effective major principal stress, and $\bar{\sigma_c}$ is the effective cohesive stress in compression, function of the accumulated equivalent plastic strain $\tilde{\varepsilon}^{pl}$, which will be defined later.

Non-associated potential plastic flow is used in the concrete damaged plasticity model. The Drucker-Prager hyperbolic function is used as flow potential G (Eq.10).

$$G = \sqrt{(\xi.\sigma_{to}.\tan\psi)^2 + \bar{q}^2} - \bar{p}.\tan\psi \tag{10}$$

Where: ψ is the dilation angle measured in the $\bar{p}$–$\bar{q}$ plane at high confining pressure; σ_{to} is the uniaxial tensile stress at failure; ξ is the eccentricity parameter.

In addition to the yield and flow potential functions, the material is characterized by stress-strain curves and damage definition in tension and compression, implemented in the model according to Eq. 11 and Eq. 13.

$$\sigma_c = (1-d)\bar{\sigma} = (1-d).D_0^{el} : \left(\varepsilon - \varepsilon^{pl}\right) = D^{el} : \left(\varepsilon - \varepsilon^{pl}\right) \tag{11}$$

$$D^{el} = (1-d)D_0^{el} \tag{12}$$

$$\varepsilon = \varepsilon^{el} + \varepsilon^{pl} \tag{13}$$

where D_0^{el} represents the initial, undamaged stiffness of the material, D^{el} indicates the degraded elastic stiffness and ε^{el} and ε^{pl} stand for the elastic and inelastic parts of the strain ε.

The tensile (σ_t) and compressive strength (σ_c) are related to the damage parameters in tension, d_t and compression, d_c as follows:

$$\bar{\sigma}_t = \frac{\sigma_t}{1-d_t} = E_0.\left(\varepsilon_t - \varepsilon_t^{pl}\right) \tag{14}$$

$$\bar{\sigma}_c = \frac{\sigma_c}{1-d_c} = E_0.\left(\varepsilon_c - \varepsilon_c^{pl}\right) \tag{15}$$

where the subscripts t and c represent the values for tension and compression, respectively, and E_0 indicates the elastic Young modulus.

Table 4 presents the plasticity input parameters utilized for the CDP model based on [27]. According to Qasem et al. [28], the dilation angle and viscosity parameter exhibit an interdependent relationship with each other and the mesh size. This study underscores the importance of systematically addressing these interactions to enhance the accuracy and reliability of numerical simulations in finite element modelling.

Table 4
Plasticity input parameters for CDP.

Parameter	Dilatation angle	Eccentricity	σ_{b0}/σ_{c0}	K_c	Viscosity parameter
Value	38	0.1	1.07	0.6667	0.0001 [28]

4.1.1. Compression and tension of UHPFRC

The uniaxial compressive stress-strain relationship of the UHPFRC used in this study was based on the constitutive equations proposed by Krahl et al. [27] as expressed in Eq. 16 and Eq. 19.

$$\sigma_c = \sigma_0\left[\frac{k_1\beta\frac{\varepsilon}{\varepsilon_0}}{k_1\beta - 1 + \left(\frac{\varepsilon}{\varepsilon_0}\right)^{k_2\beta}}\right] \tag{16}$$

$$\beta = \frac{1}{1 - \frac{\sigma_0}{\varepsilon_0 E_{c0}}} \tag{17}$$

$$k_1 = 0.42539 - 0.004942\beta - 0.2071W_c + 0.00186\beta^2 + 0.16163W_c^2 \tag{18}$$

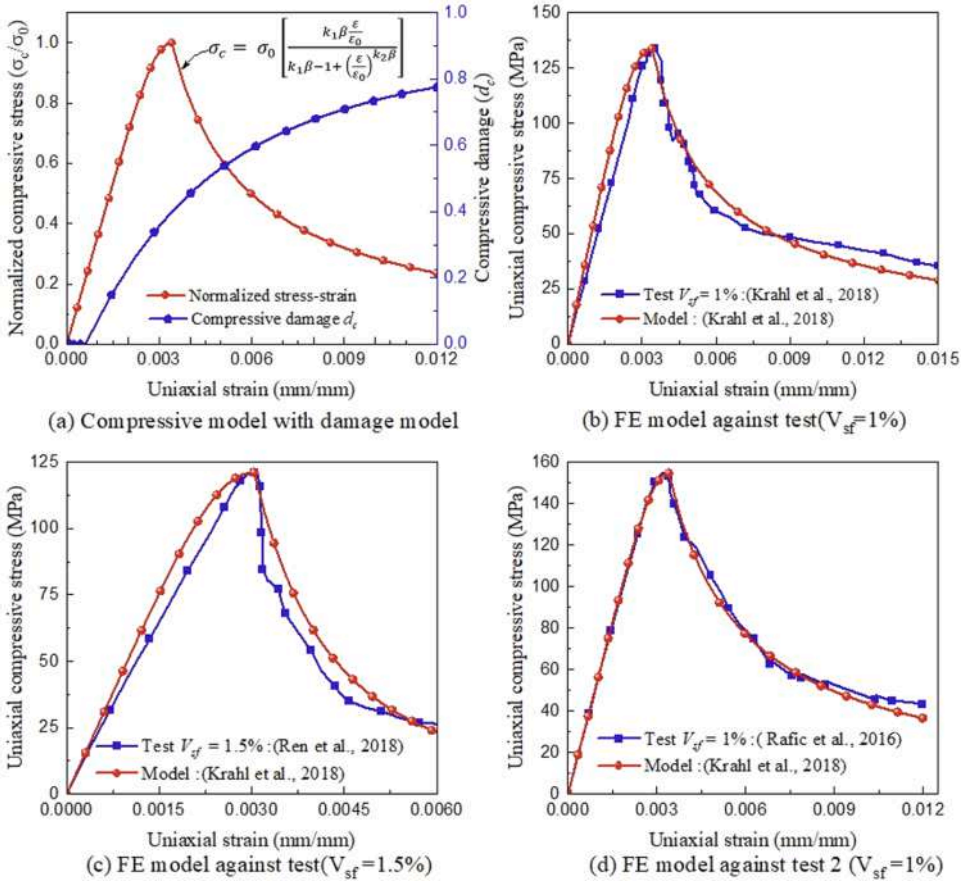

Fig. 15. Compressive constitutive model comparison with previous test data.

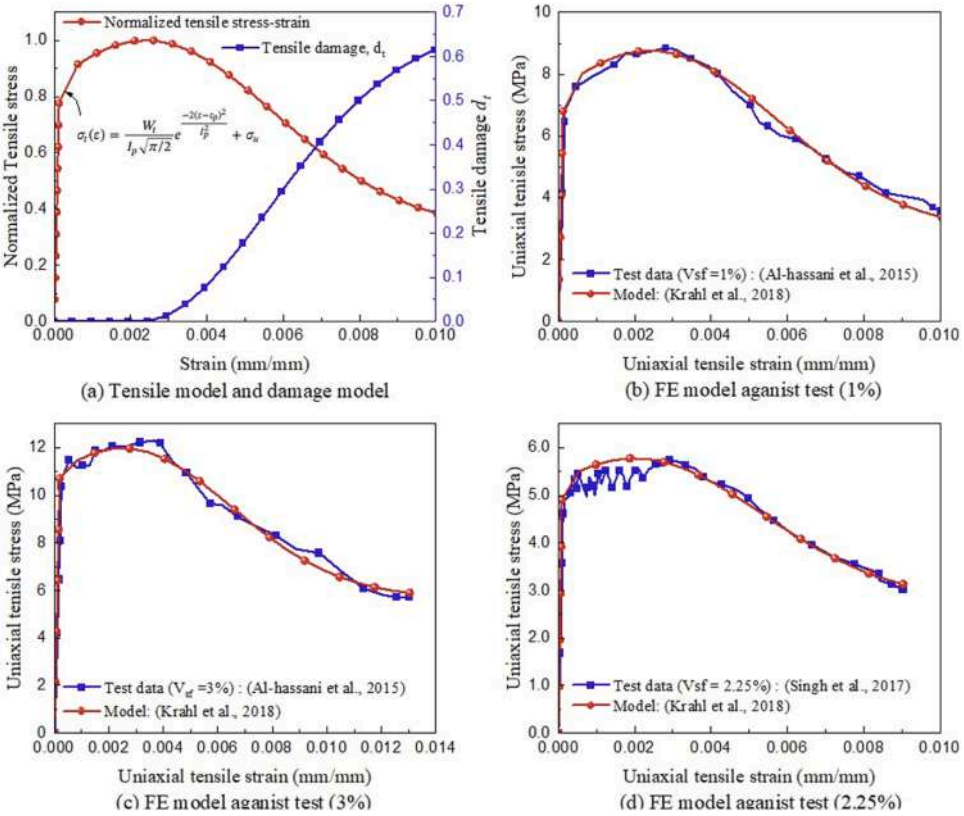

Fig. 16. Tension constitutive model comparison with previous test data.

Table 5
Properties of the EPS foam.

Density (kg/m^3)	Young's Modulus (MPa)	Poisson's ratio	Compression yield stress ratio	Plastic passion ration
12.75	2.2	0	1	0.1

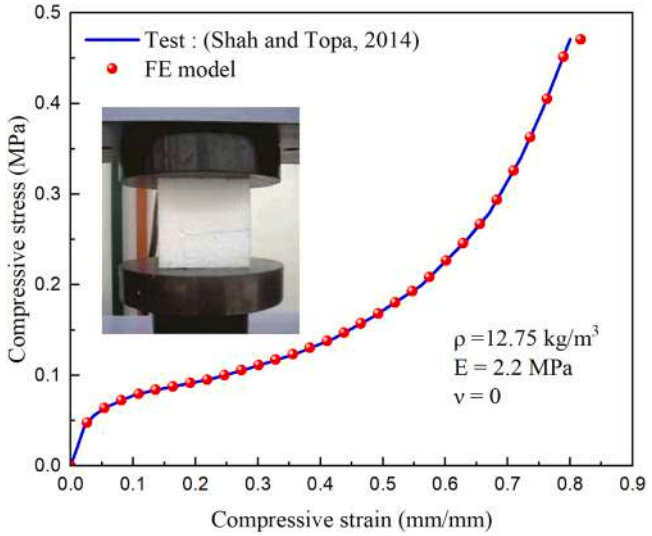

Fig. 17. Experimental and predicted response of EPS using Crushable foam model.

$$k_2 = 1.19603 - 0.09059\beta - 0.82313W_c + 0.00329\beta^2 + 0.37862W_c^2 \tag{19}$$

Where σ_0, ε_0, E_{c0} are the peak stress, peak strain and initial modulus of elasticity, respectively. k_1 and k_2 are experimental-based parameters relative to the post-peak range of experimental results. k_1 and k_2 were calibrated for the parameters β and the total energy W_c that is equal to the mean area of the experimental stress-strain curves.

The uniaxial constitutive model proposed by Krahl et al. [27] for the UHPFRC compression response is shown in Fig. 15(a), along with the damage degradation model. The capability of this model was compared with experimental data from several studies [27,29,30] for 1 % and 1.5 % steel fibre ratios, demonstrating its ability to closely replicate the experimental compressive stress-strain behaviour, as shown in Fig. 15 (b-d). The proposed model effectively captures the stress-strain response of UHPFRC across different datasets. The damage variable in Fig. 15(a) increases with strain, indicating progressive material stiffness degradation.

The tensile constitutive model, characterized by nonlinear hardening and softening as proposed by Krahl et al. [27] (Eq. 20), was adopted in this study due to its demonstrated ability to capture the experimental stress-strain behaviour of UHPFRC. Fig. 16(a) illustrates this constitutive model along with the associated tensile damage degradation.

$$\sigma_t(\varepsilon) = \frac{W_t}{I_p\sqrt{\pi/2}} e^{\frac{-2(\varepsilon - \varepsilon_p)^2}{I_p^2}} + \sigma_{rt} \tag{11′}$$

Where W_t is the total energy measured under the tensile stress-strain curve; I_p is the inflection point of the curve at the descending branch; ε_p is the peak tensile strain, σ_{rt} is the residual tensile strain.

Fig. 16 (b-d) shows the comparison of the constitutive tensile model with experimental data from [27,31]. Fig. 16 (a) illustrates the normalized tensile stress-strain response along with the tensile damage evolution (d_t). The model captures the initial elastic behavior, strain-hardening, and strain-softening phases. The damage variable (d_t) increases with strain, representing the progressive degradation of material stiffness. The comparison shows the ability of the tensile constitutive model to predict the tensile stress-strain of UHPFRC accurately.

4.1.2. EPS modelling

The crushable foam mode in FE software was used to model the EPS response. This material model required the input of five parameters: density of material, modulus of elasticity, Poisson's ratio, and stress-strain hardening, as given in Table 5. This model was compared with experimental data from [23].

A Comparison between the experimental and simulation results shows the capability of the model to reproduce the stress-strain curve with excellent match, as shown in Fig. 17. Therefore, the calibrated material parameters and model used are capable of accurately predicting the response of EPS crushable foams.

4.2. Interaction Interface

To simulate the interaction between the UHPFRC floodwall and the EPS foam core, a surface-based interaction algorithm was employed. In this model, the tangential behaviour was defined using a penalty friction

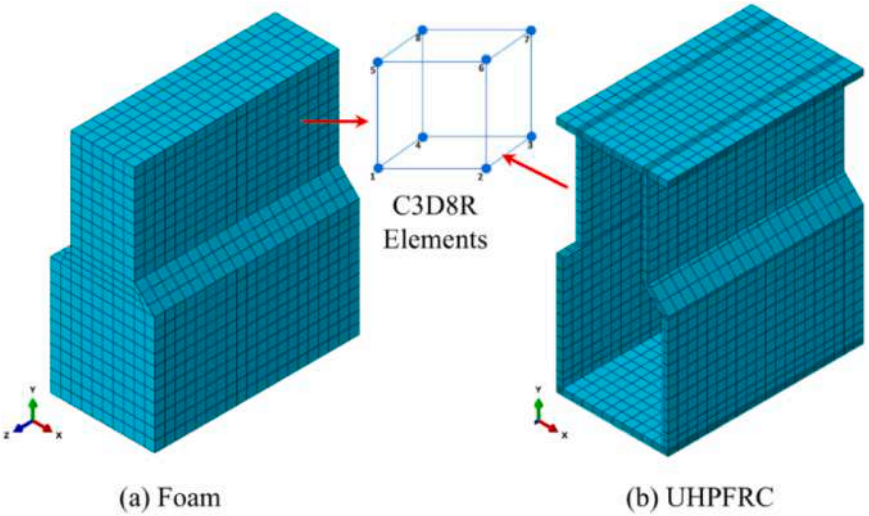

Fig. 18. Mesh of the FE model.

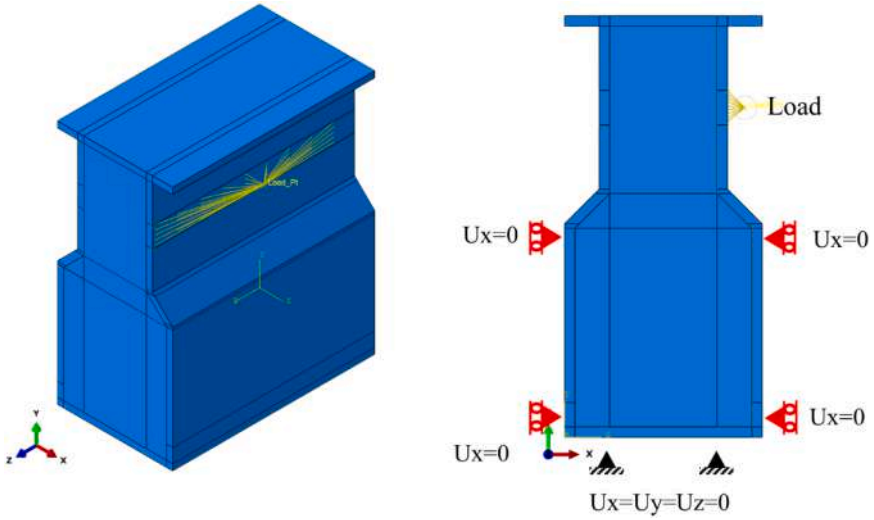

Fig. 19. Load and boundary conditions on FE model.

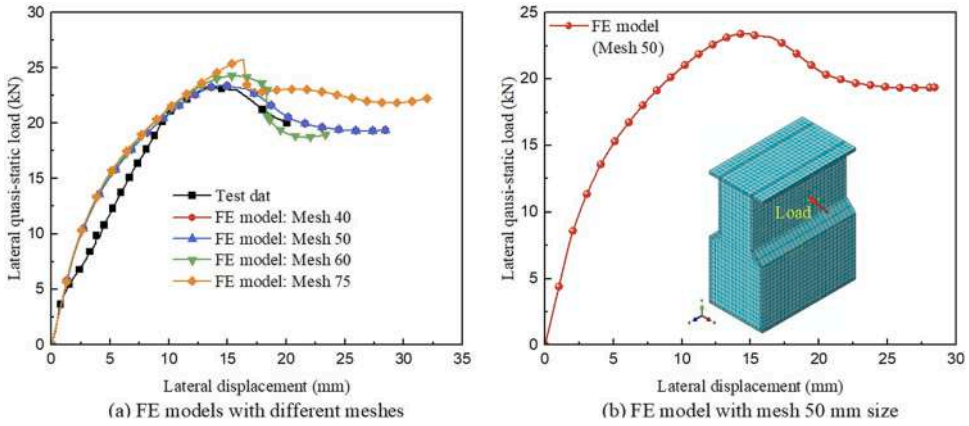

Fig. 20. Load-displacement response.

formulation with a coefficient of 0.2. This approach is consistent with previous studies [32–34], where the interface between concrete and foam is typically characterized by a weak bond and is effectively represented using low-coefficient frictional contact.

4.3. Mesh and element type

The 8-node 3D solid element with reduced integration (C3D8R) was used to model the UHPFRC and EPS parts. Fig. 18 (a) and (b) shows the mesh details for UHPFRC floodwall and infilled EPS, respectively.

4.4. Load and boundary conditions

The FE model was developed to replicate the behaviour of the sandwich floodwall under the quasi-static lateral load and boundary conditions implemented during the actual test. Fig. 19 illustrates the FE model's load and boundary conditions. The boundary and load conditions were applied to the FE model in the same way they were implemented during the experimental test, as shown in Fig. 9. The bottom of the wall was restrained against translations in all directions. At 100 mm height and 600 mm height, the translation in the x-direction, representing the wall setup during a flooding event, was restrained (Fig. 2). An equivalent hydrostatic pressure was applied at a height of 945 mm from the wall base via a reference point connected to the loading surface through coupling constraints (Fig. 19), ensuring uniform load transfer over the surface without inducing stress localization.

Table 6
FE and experimental comparison of lateral yield and ultimate load-displacement parameters.

Parameter	Experimental test	FE model	Variation (%)
Lateral yield load (kN)	21.07	20.15	4.4
Lateral yield displacement (mm)	10.16	9.18	9.6
Lateral ultimate load (kN)	23.36	23.41	0.21
Lateral ultimate displacement (mm)	13.36	14.28	7

5. FE results verification

The FE results obtained were compared with the experimental results for the floodwall specimen based on the load–displacement response and cracking pattern.

5.1. Load versus displacement response

The lateral load–displacement responses from FE analyses using mesh sizes of 40 mm, 50 mm, 60 mm, and 75 mm were compared with experimental data (Fig. 20(a)). Meshes of 40 mm and 50 mm closely matched the experimental curve, while coarser meshes (60 mm and

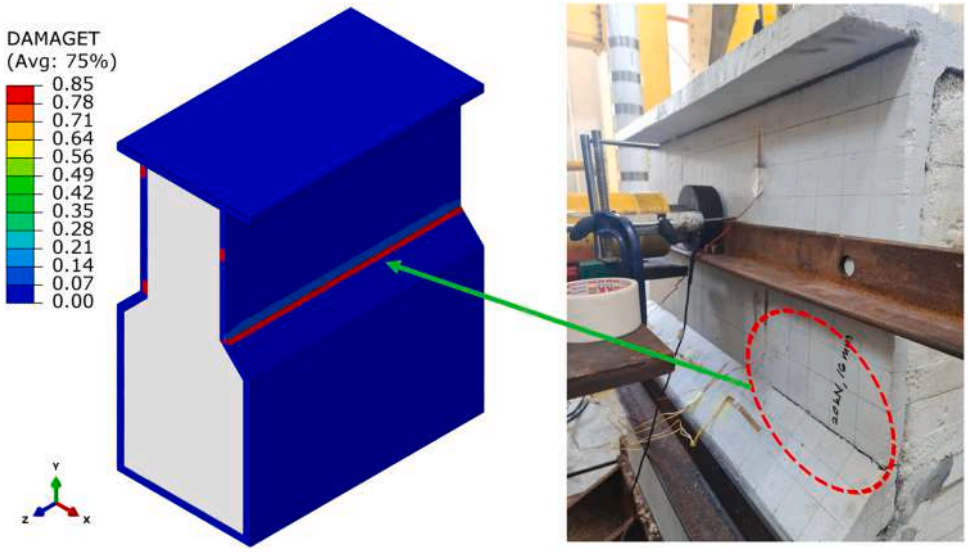

Fig. 21. FE and experimental crack distribution comparison.

75 mm) overestimated the peak load and post-peak behaviour, supporting the selection of the 50 mm mesh size.

Further examining the mesh, the FE model with a 50 mm mesh size was identified as the appropriate size to achieve accuracy while maintaining computational efficiency. Examining the curve, the FE model results exhibited good agreement with the experimental results. The FE curve agreed well with the experimental results in the plastic region; however, it showed slightly stiffer behaviour than the experimental curve in the elastic region. This slight difference could be due to the impact of the assumed variables and conditions in the material definition during the modelling process.

The lateral yield load and corresponding displacement listed in Table 6 were determined using the equivalent elasto-plastic yield concept [35]. This method idealizes the nonlinear structural response by replacing it with a bilinear elastic-perfectly plastic model, where the yield point marks the transition from elastic to plastic behaviour.

Referring to Fig. 20 (b), the calculated lateral yield load was 20.15 kN, which is only 4.4 % lower than the lateral test yield load (21.07 kN). The lateral yield displacement predicted by the FE model was 9.18 mm, which was 9.6 % lower than the lateral test yield displacement (10.16 mm). The ultimate load and corresponding displacement predicted by the FE model were 23.41 kN and 14.28 mm, respectively, which closely matched the experimental ultimate load and displacement of 23.36 kN and 13.36 mm, respectively. The comparison of the lateral ultimate load and corresponding displacement indicates that the test data differed from the FE results by 0.21 % for the lateral ultimate load and 7 % for the lateral ultimate displacement The comparison of the FE results with the experimental results for the lateral yield and ultimate loads, along with their corresponding displacements, is summarized in Table 6. Overall, based on this comparison, it can be concluded that the FE model was able to replicate the response of the floodwall subjected to lateral quasi-static load.

5.2. Cracking pattern

The FE-predicted crack distribution was compared with the experimentally observed cracking, as illustrated in Fig. 21. It can be observed that the crack propagation along the transition zone of the floodwall in the experimental test was accurately replicated by the FE model. This close alignment of the damage zones predicted by the FE model with the experimental findings indicated the accuracy of the numerical simulation in capturing the failure mechanisms of the floodwall.

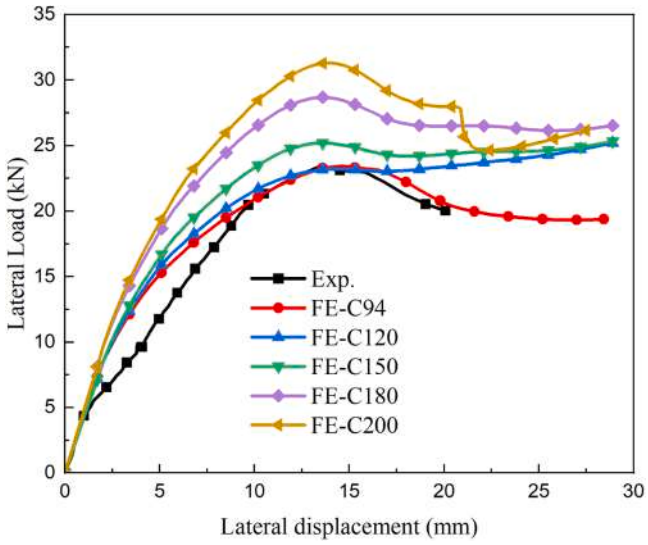

Fig. 22. Impact of UHPFRC strength on the floodwall lateral performance.

6. Parametric study

While the design configuration in Section 2 was developed based on Archimedes' buoyancy principle to ensure the floodwall remains self-floating under service conditions. However, while flotation imposes a limit on the allowable dead weight, it does not ensure adequate structural performance of the flooding wall under lateral hydrostatic pressure. Therefore, this section conducts parametric studies to evaluate how changes in key parameters, such as concrete strengths and wall thickness, affect the wall's lateral structural performance.

6.1. UHPFRC strength effect

The floodwall response was predicted by the FE model with different concrete strengths (94 MPa, 120 MPa, 150 MPa, 180 MPa, and 200 MPa) and compared with experimental data, as shown in Fig. 22. As validated in Section 5.1, the FE model reliably replicates the floodwall lateral behaviour.

With increasing concrete strength, the ultimate lateral load capacity improves. The FE model with 120 MPa strength (FE-C120) exhibits an

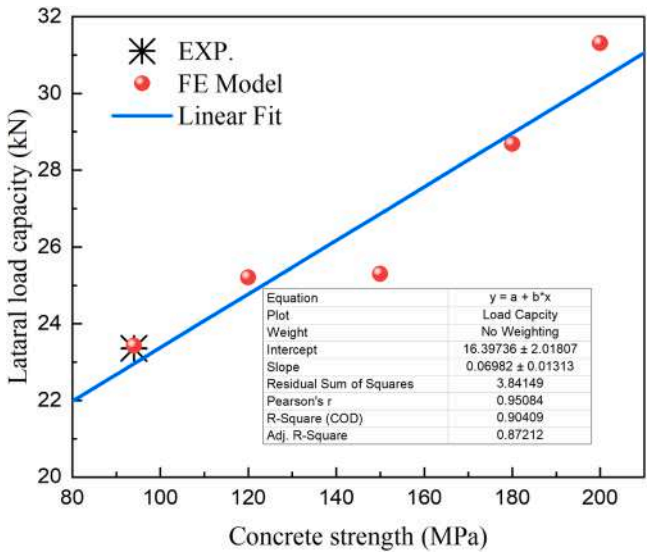

Fig. 23. Correlation between concrete strength and lateral load capacity with linear fit.

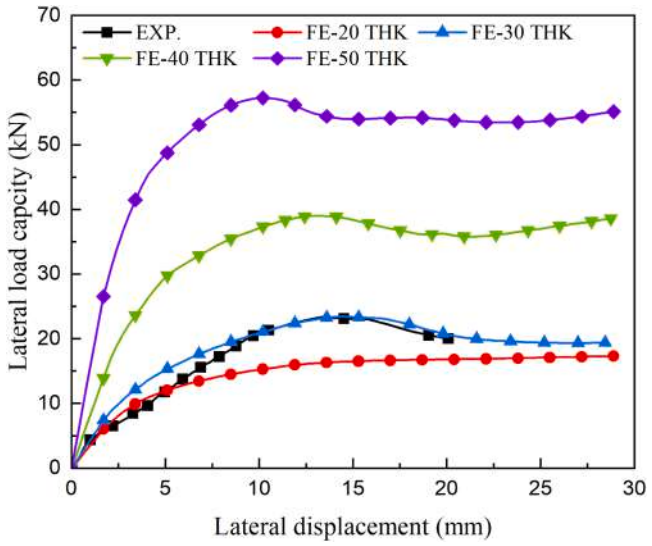

Fig. 24. Impact of wall thickness on the floodwall lateral performance.

increase in lateral load beyond the peak capacity of FE-C94, showing an enhancement in performance. With 150 MPa strength (FE-C150), the ultimate lateral load reaches 25.3 kN, representing an 8.3 % improvement over FE-C94. Similarly, for 180 MPa (FE-C180) and 200 MPa (FE-C200), the ultimate capacities further increase to 28.7 kN and 31.3 kN, respectively, corresponding to 23 % and 34 % improvements compared to the 94 MPa case.

However, for 200 MPa concrete strength, the post-peak response shows a gradual load decrease, indicating ductile failure behaviour. This suggests that while higher concrete strength improves load-bearing capacity, it does not compromise ductility, and the structure remains capable of sustaining loads beyond the peak without sudden failure.

The effect of UHPFRC strength on the lateral performance of the floodwall was further examined, as shown in Fig. 23. The relationship between UHPFRC strength and lateral load capacity appears to be fairly linear, as indicated by the high R^2 value (0.90409) and Pearson's correlation coefficient (0.95084), suggesting a strong correlation.

Overall, increasing UHPFRC strength consistently enhances the floodwall's lateral load capacity while maintaining ductile behaviour,

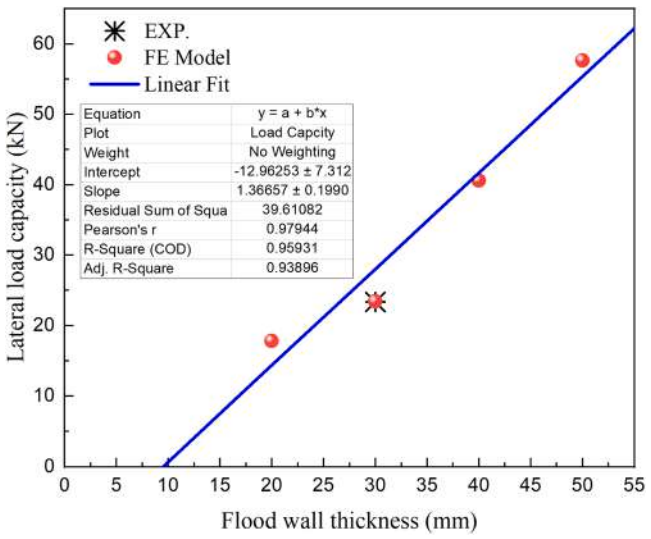

Fig. 25. Correlation between floodwall thickness and lateral load capacity with linear fit.

demonstrating a strong and nearly linear correlation between concrete strength and structural performance.

6.2. *Wall thickness effect*

The effect of floodwall thickness on its lateral load performance was analysed using an FE model with thicknesses of 20 mm, 30 mm, 40 mm, and 50 mm. The lateral load–lateral displacement responses of both the experimental and FE models are shown in Fig. 24. The floodwall with a thickness of 20 mm exhibited the lowest lateral capacity of 17.81 kN, which was 24 % lower than the experimental test result for the 30 mm wall. Furthermore, the FE-20THK model showed no significant capacity increase beyond 16.37 kN, corresponding to a displacement of 13.94 mm. Increasing the thickness to 40 mm significantly enhanced the lateral performance, demonstrating improved elastic and inelastic behaviour compared to the 30 mm model. The lateral capacity of the FE-40THK model (40.58 kN) was 73 % higher than that of the FE-30THK model (23.36 kN). A further increase in thickness to 50 mm led to a substantial improvement in lateral response, with the FE-50THK model reaching a capacity of 57.62 kN—146 % higher than FE-30THK and 42 % higher than FE-40THK. This highlights that a 10 mm increment in UHPFRC wall thickness has a significant impact on performance, demonstrating the material's high strength even with minimal geometric changes.

Again, the relationship between the wall thickness and the lateral load capacity was also examined as shown in Fig. 25. The figure illustrates a consistent increase in lateral load capacity with floodwall thickness, demonstrating a strong linear relationship ($R^2 = 0.959$). The high Pearson's correlation coefficient (0.9794) further confirms this trend, indicating minimal deviation across the data points. The trend confirms that increasing floodwall thickness significantly enhances lateral load resistance, supporting the material's high strength-to-thickness efficiency.

7. Conclusion

This study presents a novel self-rising floodwall system (SRFS) designed to provide efficient flood protection through a buoyancy-driven activation mechanism. The developed system consists of a thin ultra-high-performance fibre-reinforced concrete (UHPFRC) shell (30 mm) enclosing a hollow core filled with expanded polystyrene (EPS) foam, ensuring structural integrity while minimizing weight. This optimized design configuration ensures a balance between strength,

durability, and buoyancy, making the SRFS a viable solution for automatic flood mitigation.

The buoyancy test results confirm that the developed floodwall design achieves the intended self-rising functionality by generating adequate uplift force to lift its weight. Despite the constraints of the test setup, the displaced level of 200 mm for the wall demonstrates this developed system's ability to work as intended, confirming the effectiveness of its buoyancy-driven activation mechanism in this SRFS.

The experimental investigation demonstrated that the SRFS operates effectively without external power, floating in response to rising water levels and providing significant resistance to hydrostatic pressure. The lateral quasi-static load test confirmed the floodwall's excellent performance to resist the flooding water, with a maximum load capacity of 23.36 kN which is double the design strength of the flood resistance.

The validated FE models closely matched the experimental data, confirming their accuracy in simulating the SRFS response.

The parametric analyses revealed that increasing UHPFRC strength enhances the floodwall's lateral resistance. Specifically, increasing the concrete strength from 94 MPa to 150 MPa, 180 MPa, and 200 MPa improved the ultimate lateral load capacity by 8.3 %, 23 %, and 34 %, respectively. Additionally, increasing the wall thickness from 30 mm to 40 mm and 50 mm significantly improved lateral hydrostatic resistance by 73 % and 146 %, respectively. These findings show a linear correlation between concrete strength, wall thickness, and lateral load capacity.

Overall, the findings highlight the SRFS's potential as an effective, self-activating flood protection system, offering enhanced structural resilience, minimal maintenance requirements, and suitability for diverse flood mitigation applications.

CRediT authorship contribution statement

Arash Rahmatian: Writing – review & editing, Supervision, Methodology, Investigation, Formal analysis, Data curation, Conceptualization. **Raizal Saifulnaz Muhammad Rashid:** Writing – review & editing, Supervision, Resources, Funding acquisition. **Farzad Hejazi:** Writing – review & editing, Visualization, Validation, Supervision, Resources, Project administration, Methodology, Investigation, Funding acquisition, Formal analysis, Data curation, Conceptualization. **Benidir Rima:** Writing – original draft, Validation, Supervision, Software, Methodology, Investigation, Formal analysis, Data curation.

Declaration of Competing Interest

The authors declare that they have no known competing financial interests or personal relationships that could have appeared to influence the work reported in this article.

References

[1] Muñoz-Caballero J, Vergara D, Fernández-Arias P, Antón-Sancho Á. Design of a smart barrier to internal flooding. Inventions 2022;7. https://doi.org/10.3390/inventions7040088.

[2] Janssen SKH, van Tatenhove JPM, Mol APJ, Otter HS. Greening flood protection through knowledge processes: lessons from the markermeer dikes project in the Netherlands. Reg Environ Chang 2017;17:551–63. https://doi.org/10.1007/s10113-016-1040-1.

[3] Liem R, Köngeter J. Mobile flood protection walls: experiments and reflections on the risk of flood waves caused by a failure. Prep 21st Century 1999 WRPMD 1999: 1–10. https://doi.org/10.1061/40430(1999)108.

[4] Gupta RS, Pandule H, Bhattacharya M, Ghase P, Ingle N, Plasterwala AA. Analysis and design of flood barrier model of fabricated material. Int Res J Eng Technol 2020:1036–43.

[5] Kádár I. Mobile flood protection walls. Pollack Period 2015;10:133–42. https://doi.org/10.1556/Pollack.10.2015.1.13.

[6] Rappazzo D, Aronica GT. Effectiveness and applicability of flood barriers for risk mitigation in flash-flood prone Mediterranean area. E3S Web Conf 2016;7:3–8. https://doi.org/10.1051/e3sconf/20160712010.

[7] Wibowo JL, Ward DL. Evaluation of temporary flood-fighting structures. E3S Web Conf 2016;7:1–10. https://doi.org/10.1051/e3sconf/20160703017.

[8] Ogunyoye F., Stevens R., Underwood S. Temporary and Demountable Flood Protection Guide protecting and improving the environment in England and. 2011.

[9] Haaland KV. Prototyping and testing of novel flood protection systems. Norwegian University of Science and Technology; 2016.

[10] Strømsnes S. Concept development of all-new flood protection system. Norwegian University of Science and Technology; 2015.

[11] Chen S, Li H, Guo L, Wang L, Cao Y. Testing the key performance of mobile flood protection system. Adv Civ Eng 2018;2018:1–11. https://doi.org/10.1155/2018/5641385.

[12] Wali UG, Munyaneza O, Nzeyimana YK. Hydraulic structures design for flood control in the nyabugogo wetland, Rwanda. Nile Basin Water Sci Eng J 2013;6:26–37.

[13] Maryamh K, Glock C. Lautern barrier - innovative self-closing flood protection system from UHPFRC. Beton Und Fert Plant Precast Technol 2020;86:42–51.

[14] Mario J, Baiz C. STRUCTURAL RESPONSE OF SMART WALLS by. State University of New York at Buffalo in; 2016.

[15] Krishnan L, Mugesh A, Pradeep Kumar S, Manivannan R. Analytical study on self closing flood barrier using ANSYS. Int J Eng Res Technol 2018;3:1–4.

[16] AZM Al-qaisi, AMA Al-rammahi. Optimum shape of concrete flood walls under hydrodynamic load. J Univ Kerbala 2017;15:141–54. https://doi.org/10.13140/RG.2.2.15179.85280.

[17] Petrů M, Srb P, Ševčík L, Lufinka A. Testing and numerical analysis of mechanical stress mobile flood barriers. EAN 2017 55th Conf Exp Stress Anal 2017 2017;1:350–3.

[18] Petru M, Srb P, Sevcik L, Martinec T, Kulhavy P. Development of an anti-flood board to protect the interiors and exteriors of the infrastructure. EPJ Web Conf 2018;180:4–7. https://doi.org/10.1051/epjconf/201817002083.

[19] Srb P, Petru M, Kulhav P. Numerical simulation of flood barriers. EPJ Web Conf 2017;143:1–6. https://doi.org/10.1051/epjconf/201714302115.

[20] Lazarus Dachollom G, Hejazi F, Yusuf B. Development of ultra High-Performance fiber reinforced concrete barge for 5 MW wind turbine. Structures 2023;53:1349–68. https://doi.org/10.1016/j.istruc.2023.04.113.

[21] AFGC. Ultra High Performance Fibre-Reinforced Concretes. 2013.

[22] Graybeal B. Technote-Ultra-High Performance Concrete. 2011.

[23] Shah QH, Topa A. Modeling large deformation and failure of expanded polystyrene crushable foam using LS-DYNA. Model Simul Eng 2014;2014. https://doi.org/10.1155/2014/292647.

[24] Dassault Systèmes. Abaqus 6.11,Analysis User's Manual. vol. III. 2011.

[25] Lubliner J, Oliver J, Oller S, Onate E. A Plastic-Damage model. Int J Solids Struct 1989;25:299–326.

[26] Lee J, Fenves GL. Plastic-Damage model for cyclic loading of concrete structures. J Eng Mech 1998;124:892–900.

[27] Krahl PA, Carrazedo R, El Debs MK. Mechanical damage evolution in UHPFRC: experimental and numerical investigation. Eng Struct 2018;170:63–77. https://doi.org/10.1016/j.engstruct.2018.05.064.

[28] Qasem M, Hasan M, Muhamad R, Chin CL, Alanazi N. Generalised calibration and optimization of concrete damage plasticity model for finite element simulation of cracked reinforced concrete structures. Results Eng 2025;25:103905. https://doi.org/10.1016/j.rineng.2024.103905.

[29] Ren GM, Wu H, Fang Q, Liu JZ. Effects of steel fiber content and type on static mechanical properties of UHPCC. Constr Build Mater 2018;163:826–39. https://doi.org/10.1016/j.conbuildmat.2017.12.184.

[30] El-Helou RG, Haber ZB, Graybeal BA. Mechanical behavior and design properties of Ultra-High- performance concrete. Acids Mater J 2022;119:181–94. https://doi.org/10.14359/51734194.

[31] M. Al-Hassani H, I. Khalil W, S. Danha L. Proposed model for uniaxial tensile behavior of ultra high performance concrete. Eng Technol J 2015;33:61–77. https://doi.org/10.30684/etj.33.1a.5.

[32] Jawdhari A, Fam A. Thermal-Structural analysis and thermal bowing of double wythe UHPC insulated walls. Energy Build 2020;223:110012. https://doi.org/10.1016/j.enbuild.2020.110012.

[33] Kadhim MMA, Jawdhari A, Fam A. Design equations for thermal bowing and composite degree of concrete sandwich panels. Eng Struct 2023;290:116341. https://doi.org/10.1016/j.engstruct.2023.116341.

[34] Huang JQ, Dan ML, Chong X, Jiang Q, Feng YL, Wang YW. Out-of-plane shear performance of textile reinforced concrete sandwich panel: numerical analysis and parametric study. Structures 2025;71:108080. https://doi.org/10.1016/j.istruc.2024.108080.

[35] Park. Structural assemblages from laboratory testing. NZSEE N Zeal Soc Earthq Eng 1989;22:155–66.